

# THE 4TH INTERNATIONAL CONFERENCE ON ALUMINUM ALLOYS

## STUDY AND ANALYSIS OF MICROSCOPICAL MECHANISMS RESPONSIBLE FOR FATIGUE DAMAGE IN 7010 ALUMINUM ALLOY

G. Petton<sup>1</sup>, C. Rinaldi<sup>2</sup> and R. Fougères<sup>1</sup>

1. GEMMPPM, URA CNRS n°341, INSA-Lyon Bât. 303. 20, avenue Albert Einstein, F-69621 Villeurbanne Cedex - France

2. ENS Mines de Saint-Etienne, Centre SMS, Microstructures et Mise en Forme, 158 Cours FAURIEL, F-42023 S<sup>L</sup>-ETIENNE Cedex 2 - France

### Abstract

Study of fatigue damage in high strength aluminum alloy 7010 at T7651 temper was realized. A mesoscopic approach using optical and SEM techniques yielded the damage chronology during cycling. Fatigue crack initiation sites are found to be Al<sub>7</sub>Cu<sub>2</sub>Fe or Mg<sub>2</sub>Si intermetallic clusters at or close to the surface. The macroscopic propagation direction of the fatigue crack is perpendicular to the tensile axis chosen parallel to the transverse direction. Fatigue crack path can be intergranular and transgranular whatever the local recrystallization state, a mixed grain structure of unrecrystallized and recrystallized grains existing within the material. A crack percolation phenomenon leads to the final fracture.

Initiation sites can be explained through elastic and plastic strain incompatibilities of the microheterogeneity with the matrix. So, additional techniques were used such as nanoindentation to get the Young's modulus of the intermetallics and Atomic Force Microscopy to evaluate the plastic strain within the matrix. In order to check whether a correlation exists with the local texture, crystallographic orientations around initiation sites were obtained by Electron Backscattering Diffraction in SEM.

### Introduction

Fatigue behavior of 7010 aluminum alloy was already investigated elsewhere [1-6]. As a matter of fact, crack growth data ( $da/dN$  versus  $\Delta K$ ) and fractography analysis (striation spacings) can be found. However, damage chronology is not explicitly described. In this paper, thanks to a mesoscopic approach, we are able to describe the damage chronology which is required prior to any modelization. Additional experiments are also presented in order to evaluate parameters needed for fatigue quantification.

### Material and experimental conditions

The 7010 alloy composition is given in Table I and the heat treated conditions we investigated is over-aged : T7651. The material exhibits two grain families, the recrystallized and the unrecrystallized ones [7], the sizes of which being given in Table II. Within the latter grain family one can find subgrains which are rather equiaxed (figure 1). Otherwise the grains have usual pancake shape of aluminum alloy belonging to the 7000 series [8]. The unrecrystallized grains may be considered as cells surrounded by the recrystallized grains which may be seen as walls.

Table I. Composition of 7010 Aluminum alloy (% weight)

Zn	Mg	Cu	Zr	Fe	Si	Ti
6.07	2.43	1.60	0.103	0.098	0.079	0.028

Table II : Grain sizes of 7010-T7651 aluminum alloy

	Long direction	Transverse direction	Normal direction
Unrecrystallized grains	350 $\mu\text{m}$	150 $\mu\text{m}$	60 $\mu\text{m}$
Equiaxed subgrains		2 to 5 $\mu\text{m}$	
Recrystallized grains	80 $\mu\text{m}$	60 $\mu\text{m}$	40 $\mu\text{m}$

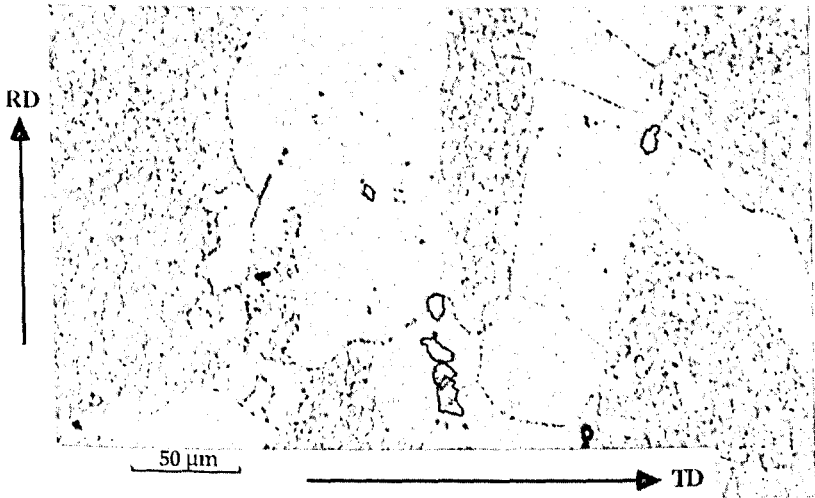


Figure 1. Optical micrograph of 7010-T7651 aluminum alloy

The intermetallics which can be found within the material are mainly  $\text{Al}_7\text{Cu}_2\text{Fe}$  and  $\text{Mg}_2\text{Si}$ . The  $\text{Mg}_2\text{Si}$  phase exhibits a rather round shape while the iron secondary phase an irregular one. Their average size might estimated around 8  $\mu\text{m}$ . They gather in clusters within nearly exclusively the recrystallized grains.

The tensile axis was chosen arbitrarily parallel to the transverse direction and the maximum applied stress during cycling was either  $\sigma_{\text{max}} = 440 \text{ MPa}$ , which is nearly equal to the 0.2% proof stress, or 290 MPa. The stress ratio was always :  $R = 0.1$ . The maximum stress of 440 MPa was chosen in order to obtain the fracture at around  $10^4$  cycles and the one of 290 MPa for  $10^5$  cycles..

In order to obtain the damage chronology the surfaces of the samples were examined at different cycle number before fracture using both optical and Scanning Electron Microscopy (SEM) techniques. This procedure yielded the observation of crack initiation and propagation till the final rupture. A light etching of the surface enabled to describe the crack path.

## Results and discussion

### Damage chronology

initiation sites. The major crack initiation sites were found to be mainly due to Mg<sub>2</sub>Si or Al<sub>7</sub>Cu<sub>2</sub>Fe intermetallic fracture (figure 2). Some minor initiation sites might be Mg<sub>2</sub>Si/matrix interface decohesion and grain boundary decohesion. The intermetallic clusters in which the cracks appeared were close to the free surface as it can be observed in figure 3 thanks to the SEM-Backscattering Electron Image in composition contrast realized on a fracture surface.

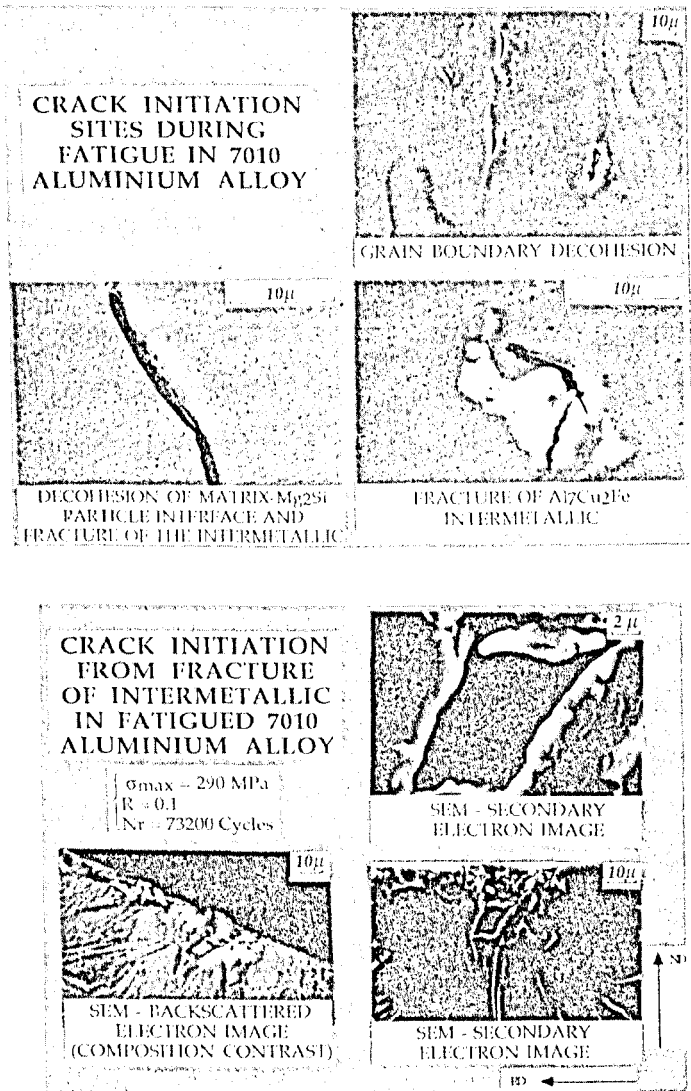


Figure 3. Fractography showing crack initiation in an intermetallic cluster

In addition, all the long cracks we observed on the free surface before fracture exhibited

intermetallics in the middle. A tilted view after fracture allowed verification that the assumed initiation sites were the actual ones. On the same sample several initiation sites might be generated and it seems that microcracks appear rather lately. Indeed, the ratio of the crack initiation cycle number over the rupture cycle number seems to be greater than 0.8 .

Crack growth. From a macroscopical point of view the crack propagation occurs in mode I (Figure 4). However, locally the crack path, revealed by chemical etching, can have a zigzag shape following intergranular, transgranular, inter-subgranular or even sometimes trans-subgranular path (see for example figure 5). The intergranular path may be either along recrystallized/recrystallized grain boundaries or recrystallized/unrecrystallized grain boundaries. So, according to the microstructure all local fatigue crack paths are possible.

Percolation phenomenon. Since several macrocracks can exist the question is whether only one crack grows up leading to the final rupture or the macrocracks join together. All the macrocracks were observed on the surfaces of a sample before rupture in order to be able to follow their propagation. After rupture, the fracture surface profile showed that two macrocracks joined together. In addition, fractography observations showed two distinct initiation sites.

Figure 4. A long fatigue crack observed on the sample surface at  $N=17349$  cycles ( $N_r = 18523$  cycles)



10  $\mu$ m



Figure 5. Detail of figure 4 showing the crack initiation site and local crack paths

## Fatigue crack initiation analysis

Role of elastic and plastic strain incompatibilities. As soon as the elastic strain energy,  $W_{el}$ , stocked within an heterogeneous particle embedded in an infinite matrix reaches the critical value of :  $2 \gamma S$ ,  $\gamma$  being the fracture surface energy and  $S$  the area of the surface to be created, crack initiation occurs. Usually  $S = \pi a^2$  with  $a$  the radius of the particle assumed as spheroidal. Taking into account only elastic and plastic strain incompatibilities between the particle and the matrix, the energy  $W_{el}$  can be written [9] :

$$W_{el} = \frac{V_I}{2} [ \sigma_{ij}^A ( \epsilon_{ij}^A + \epsilon_{ij}^{ATeq} ) - \sigma_{ij}^I \epsilon_{ij}^{PTeq} ] \quad (1)$$

with  $V_I$  the volume of the particle and :

- \*  $\sigma_{ij}^A$  the applied elastic stress field :  $\sigma_{ij}^A = C_{ijkl} \epsilon_{ij}^A$ ,  $C_{ijkl}$  the elastic constants of the matrix
- \*  $\epsilon_{ij}^{ATeq}$ , the stress free strain tensor for the equivalent particle resulting from the elastic strain incompatibilities
- \*  $\sigma_{ij}^I$  particle internal stresses due to plastic strain incompatibilities
- \*  $\epsilon_{ij}^{PTeq}$  the stress free strain tensor for the equivalent particle resulting from the plastic strain incompatibilities elastically relaxed

In order to be able to compute  $W_{el}$ , additional experiments have to be performed to evaluate elastic strain incompatibility contribution :  $E1 = \frac{V_I}{2} \sigma_{ij}^A \epsilon_{ij}^{ATeq}$ , and plastic strain

incompatibility contribution :  $E2 = \frac{V_I}{2} \sigma_{ij}^I \epsilon_{ij}^{PTeq}$  to the total elastic strain energy. As a matter of fact, the former term  $E1$  is proportional to the difference of Young's moduli of the two phases which implies the measurements of the Young's moduli. The latter term  $E2$  requires the determination of the average plastic strain within the matrix which can be done by Atomic Force Microscopy.

→ Young's modulus So, in order to quantify the elastic strain incompatibility we need to know the Young's moduli of the microheterogeneities and the matrix. The Young's moduli were obtained using a nanoindenter [10]. The values for Mg<sub>2</sub>Si phase exhibited a high dispersion with a tendency to be lower than the ones of the matrix. The Young's modulus of the Al<sub>7</sub>Cu<sub>2</sub>Fe intermetallic is given in Table III and we see that it is nearly twice as high as the one of the matrix.

Table III. Young's moduli by nanoindentation technique

	Applied force (mN)	Mean penetration depth (nm)	Young's modulus (GPa)
Matrix	3	269.2	72.3 ± 2
Al <sub>7</sub> Cu <sub>2</sub> Fe intermetallic	3	137.7	148.4 ± 7

The elastic strain incompatibility contribution in term of energy was computed for a spheroidal Al<sub>7</sub>Cu<sub>2</sub>Fe particle with a radius of 4 μm and with an applied stress of 440 MPa. We found :

$$E1 = \frac{V_I}{2} \sigma_{ij}^A \epsilon_{ij}^{ATeq} = 2.48 \cdot 10^{-10} \text{ J} \quad (2)$$

→ Atomic Force Microscopy. In order to compute the plastic strain contribution to  $W_{el}$ , (equation 1) the average plastic strain of the matrix has to be measured. We used an Atomic Force Microscope to get the average heights ( $h$ ) and widths ( $w$ ) of the slip bands on the

surface of a reference and fatigued sample (Figure 6). The cross section of the fatigue sample showing extrusions and intrusions presented in figure 6 was obtained for a grain close to the fracture surface. This means that we got the maximum value of the slip band height and the maximum value of the shear plastic strain which is to exist within the matrix. We found :  $h \approx 20 \text{ nm}$  and  $w \approx 2 \mu\text{m}$ . Thus, the maximum shear plastic strain might be taken as :  $\gamma_p = \frac{h}{w} \approx 1\%$ . Using the same values as in equation 2 :

$$E_2 = \frac{V_I}{2} \sigma_{ij}^I \varepsilon_{ij}^{PTeq} = 11.12 \cdot 10^{-10} \text{ J} \quad (3)$$

So, if we compare  $E_1$  with  $E_2$  we see that the plastic strain incompatibilities are far from being negligible since the corresponding energy  $E_2$  is higher than  $E_1$  :  $E_2 \approx 4.49 E_1$ . Therefore, we see that for the crack initiation energy criterion the plastic strain incompatibility term has to be taken into account and that the measurement of the plastic strain in the matrix has to be done. Nevertheless, for a lower applied stress the elastic strain incompatibility contribution should be enhanced in comparison with the plastic strain incompatibility one. In addition, we can notice that if a local plastic relaxation of the plastic strain incompatibilities around the intermetallics is to exist the energy term  $E_2$  would be decreased.

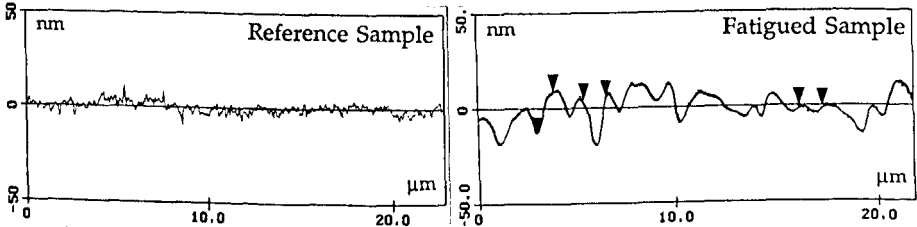


Figure 6. Height and width of slip bands obtained by Atomic Force Microscopy

Role of Local texture on fatigue crack initiation. Local crystallographic grain orientations around particles are likely to play an important role on crack initiation. In order to verify if such an influence exists, we used Electron Backscattering Diffraction technique (EBSD) in a SEM to get (001) pole figures of the grains around broken intermetallics which created short fatigue cracks. The pole figures were obtained in a macroscopic axis reference linked to the sample and tensile axes.

In the example we present in figure 7, a broken  $\text{Mg}_2\text{Si}$  intermetallic was embedded in a recrystallized grain. In order to know the actual crack plane the sample was cut along a plane perpendicular to the free surface and parallel to the tensile axis. This yielded a second vector belonging to the crack plane characterizing it completely. We found the crack plane to be : (010). According to Chen and Liu [11], a {100} crack plane may exist in the high strength aluminum alloys when two slip systems of two different slip planes are much more activated than the other ones. Thus, the crack plane follows alternatively the two {111} slip planes.

So, we computed the Schmid's factors in the 12 CFC slip systems (Table IV). It appeared clearly that two slip systems exhibited higher Schmid's factor values than the other ones :  $(\bar{1}\bar{1}1)[011]$  and  $(\bar{1}11)[0\bar{1}\bar{1}]$ .

Table IV. Schmid's factors in the 12 CFC slip systems

Slip system	Schmid's factor	Slip system	Schmid's factor	Slip system	Schmid's factor	Slip system	Schmid's factor
(111) $[\bar{1}\bar{1}0]$	0.328	( $\bar{1}\bar{1}1$ ) $[\bar{1}10]$	0.298	( $\bar{1}\bar{1}1$ ) $[\bar{1}\bar{1}0]$	0.286	( $\bar{1}\bar{1}1$ ) $[\bar{1}10]$	0.317
(111) $[\bar{1}0\bar{1}]$	0.099	( $\bar{1}\bar{1}1$ ) $[\bar{1}0\bar{1}]$	0.199	( $\bar{1}\bar{1}1$ ) $[101]$	0.069	( $\bar{1}\bar{1}1$ ) $[101]$	0.168
(111) $[0\bar{1}\bar{1}]$	0.228	( $\bar{1}\bar{1}1$ ) $[011]$	<b>0.496</b>	( $\bar{1}\bar{1}1$ ) $[011]$	0.217	( $\bar{1}\bar{1}1$ ) $[0\bar{1}\bar{1}]$	<b>0.485</b>

However, it is obvious that the presence of the intermetallic influences the local stress field. Using Eshelby's theory [12] the ratios of the resolved shear stresses with the applied stress were computed at any point of the intermetallic/matrix interface taking into account the ellipsoidal shape and the orientation of the particle. In this computation we took into account only the elastic strain incompatibilities. In spite of the dispersion we got in measuring the Young's modulus of the Mg<sub>2</sub>Si phase, we made the calculation using a value of 40 GPa which is lower than the value of the matrix in accordance with the tendency we had. The result was that the same two slip systems,  $(\bar{1}\bar{1}) [011]$  and  $(\bar{1}11) [01\bar{1}]$ , still showed the highest resolved shear stresses. In addition, the ratios of the the resolved shear stresses with the applied stress at different locations of the interface were higher than the corresponding Schmid's factors which means that the presence of the particle enhances local stress concentration. Computations with a higher Mg<sub>2</sub>Si Young modulus than the matrix one yielded the same two slip systems to be the most activated. Therefore, the results are in agreement with Chen and Liu [11]. We did not find a {110} crack plane like Nix and Flower [3,4,6]. Indeed, they found that fracture in 7010-T76 aluminum alloy in moist air occurred by cleavage on {110} plane.

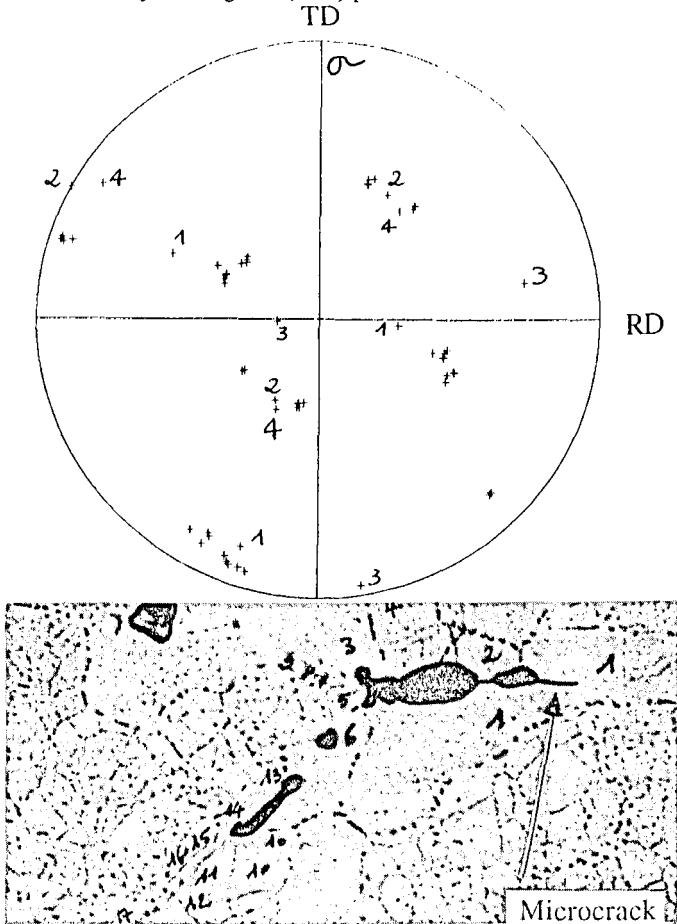


Figure 7. Crack initiation site and the corresponding (001) pole figure of surrounding grains

## Conclusions

The fatigue damage chronology of 7010-T7651 aluminum alloy can be described as follow :

- microcrack initiation by Mg<sub>2</sub>Si or Al<sub>7</sub>Cu<sub>2</sub>Fe intermetallic rupture
- macroscopic crack propagation in mode I with possible local zigzag intergranular or intragranular crack path
- final rupture through a percolation phenomenon

Young's modulus of the Al<sub>7</sub>Cu<sub>2</sub>Fe intermetallics was obtained in order to evaluate the elastic strain incompatibilities between the particles and the matrix. We used an Atomic Force Microscope to measure the plastic strain within the matrix in order to compute the plastic strain contribution to the total elastic strain energy stocked within a particle. Finally, EBSD technique was used to get local texture around initiation sites for enabling the prediction of the crystallographic plane of the crack plane.

## Acknowledgments

We wish to thank the "Centre de Recherches de Voreppe" from the group PECHINEY for supplying materials and financial support.

## References

1. D. Rhodes, J. C. Radon, and L.E. Culver, Fatigue of Engineering Materials and Structures, Vol. 4, N°1, (1981), 49.
2. D. Rhodes, K.J. Nix and J.C. Radon, Proceedings of the 4th European Conference on Fracture, Leoben AUSTRIA (1982), 443.
3. K.J. Nix and H.M. Flower, Proceedings of the 5th International Conference on Fracture, Cannes FRANCE (1981), 117.
4. K.J. Nix and H.M. Flower, Proceedings of the 5th International Conference on Fracture, Cannes FRANCE (1981), 915.
5. D. Rhodes, K.J. Nix and J.C. Radon, International Journal of Fatigue, Vol. 6, N°1, (1984), 3.
6. K.J. Nix and H.M. Flower, Acta metall., Vol. 30, (1982), 1549.
13. G. Lapasset and C. Renon, La Recherche Aérospatiale, N°5, (1982), 313.
8. I. Kirman, Metallurgical Transactions, Vol. 2, (1971), 1761.
9. T. Mura, Micromechanics of defects in solids, Second edition, Dordrecht (NL) : Martinus Nijhoff Publishers, (1987), 587 pages.
10. P. Lamagnère and A. Vincent, Study of the Elastic Properties of Microheterogeneities in AISI 52100 and M50 Bearing Steels by Means of Nanoindentation, BRITE EURAM II : ELABOMM PL 5406, Reference number : ELAB T004, October 1993.
11. Q. Chen and H.W. Liu, Theoretical and Applied Fracture Mechanics, 10, (1988), 111.
12. R. Hamann, A. Mocellin, P.F. Gobin and R. Fougères, Scripta Metallurgica et Materiala, Vol. 26, N°6, (1992), 963.